

Binghamton University

The Open Repository @ Binghamton (The ORB)

Mechanical Engineering Faculty Scholarship

Mechanical Engineering

12-22-2020

Feasibility study of a micro-electro-mechanical-systems threshold-pressure sensor based on parametric resonance: experimental and theoretical investigations

Mark Pallay

Meysam Daeichin

Shahrzad Towfighian

Follow this and additional works at: https://orb.binghamton.edu/mechanical_fac



Part of the [Mechanical Engineering Commons](#)

Feasibility study of a MEMS threshold-pressure sensor based on parametric resonance: experimental and theoretical investigations

Mark Pallay, Meysam Daeichin, and Shahrzad Towfighian

Abstract—A tunable threshold pressure sensor based on parametric resonance of a microbeam subjected to electrostatic levitation is proposed. Parametric excitation can trigger a large amplitude vibration at twice the natural frequency if the magnitude of the driving force is large enough to overcome energy loss mechanisms in the system such as squeeze film damping. This causes a temporarily unstable response with a significant gain in oscillation amplitude over time until it is eventually capped by nonlinearities in the force or material or geometric properties. The instability divides the frequency region into two regions: distinct responses bounded by the system nonlinearity, and trivial responses with very low oscillation amplitudes. It is shown experimentally that the appearance of parametric resonance depends on the pressure, which influences the amount of energy loss from squeeze film damping. Therefore, the distinct difference in the vibration amplitude can be used to detect when the pressure passes a threshold level. The activation of parametric resonance also depends on the amplitude of the driving force (V_{ac}). This voltage amplitude can be set to trigger parametric resonance when the pressure drops below a predetermined threshold. A reduced-order model is developed using the Euler-Bernoulli beam theory to elucidate the nonlinear dynamics of the system. The simulation results from the mathematical model are in good agreement with the experimental data. The advantages of the proposed sensor over pull-in based sensors are its reliability and improved resolution from a large signal-to-noise ratio.

I. INTRODUCTION

Monitoring air (or other gas) pressure in many applications requires periodic checking of the pressure level to see if it has dropped below a threshold value. An example is detecting sudden changes in the air pressure inside a plane cabin to decide if breathing masks should be released for the passengers. For these applications, it would be advantageous to use a smart sensor that only triggers when the pressure drops below the specified level, eliminating the need to constantly monitor the pressure and reducing the amount of computational overhead required. One method of developing this type of smart sensor is to rely on the hysteresis in nonlinear systems, which can cause sudden changes in system dynamics when a parameter such as excitation amplitude, frequency, or damping changes. Nonlinear oscillators that are susceptible to parametric resonance are one of such systems that can trigger a significant jump in oscillation amplitude if the system damping drops below a threshold value.

Parametric excitation is a phenomenon that happens in the response of physical oscillators that have at least one of their properties varying with time [1]–[3]. For example, a simple mass-spring-damper oscillator could exhibit parametric excitation if the spring stiffness changes with time. As a result, the system will experience a dramatic change in its vibration amplitude if the magnitude and frequency of the varying stiffness satisfy the conditions needed to trigger parametric resonance. For any given system, these conditions can be found by mapping curves called transition curves in a 2D space of the magnitude and frequency of the varying parameter. If the magnitude and frequency are inside a transition curve, the system is said to be unstable and will trigger parametric resonance. These transition curves are found at numerous frequency intervals in this space, with the primary transition curve located at twice the natural frequency.

In electrostatic systems, the electrostatic force has a linear component that is proportional to the displacement of the movable electrode. This linear term acts as a second mechanical stiffness that is related to the square of the applied voltage. By applying a voltage between a fixed and movable electrode, in addition to the electrostatic force that is generated, the total effective stiffness of the movable electrode is affected. If an AC voltage with a frequency twice that of the natural frequency is applied, the system can be driven into parametric resonance. This can happen in any electrostatic system, even one that does not use a traditional parallel-plate configuration [4]. The sudden change in amplitude from parametric resonance has been exploited for sensing and actuation applications [5]–[7]. Mass and gas sensors have been developed based on parametric resonance in microstructures. [8], [9]. In a previous work, The parametric resonance for a circular micromirror is used to achieve large displacement at higher frequencies [6].

Electrostatic levitation is generated by a particular configuration of electrodes that offers several advantageous features over conventional parallel-plate-based sensors [10]–[12]. Figure 1 (a) shows the schematic of the electrode configuration in the levitation scheme. In this approach, the bias voltage is placed on the side electrodes, which are fixed to the substrate. The bottom electrode (also fixed) and the moving electrode (beam) above it are grounded. This voltage distribution creates an electrostatic force that pulls the microstructure away from the bottom electrode [11], [12].

M. Pallay, M. Daeichin, and S. Towfighian are with the Department of Mechanical Engineering, State University of New York at Binghamton, Binghamton, NY, 13902 USA, Corresponding author: S. Towfighian (stowfigh@binghamton.edu)

The nature of the electrostatic levitation force is completely different from the electrostatic force in parallel-plate capacitors, where the moving electrode is pulled toward the bottom electrode [13]. The levitation electrode configuration allows for a large vibration of the moving electrode [14] and does not suffer from the pull-in instability between the moving and bottom electrodes [15]–[17]. Furthermore, it provides the flexibility to increase the bias voltage to increase sensitivity in sensing applications [18]. The use of high bias voltages may be counted as a drawback of the levitation scheme though. However, advances in Application Specific Integrated Circuits (ASIC) designs has made handling high bias voltages possible. For some applications such as instrumentation devices, the use of high bias voltage is not of concern. In applications where the use of high bias voltages is of concern, the dimensions of the electrodes could be changed to make the use of low bias voltages feasible [14].

All MEMS (Micro-Electro-Mechanical-Systems) pressure sensors output a continuous measurement of pressure. They take advantage of linear features of MEMS such as resonance frequency of resonators [19] or deflection of a diaphragm [20] in the linear regime. This is because a linear relationship between input and output of the sensor makes the electrical circuitry and data processing much simpler [13]. Therefore, nonlinearity is undesired in pressure sensors. However, for threshold pressure sensors, exploiting nonlinear features of MEMS such as pull-in [21], buckling [22], and snap-through [23] could be very beneficial because they can improve the signal-to-noise ratio. For example, the pull-in instability of parallel-plate capacitors has been studied for threshold sensing applications [24], [25]. The dynamic pull-in of a parallel-plate capacitor depends strongly on the squeeze film damping, which is a function of pressure [26]. The main drawback of this approach is that pull-in may cause permanent failure of the device with a detrimental effect on its reliability [27]. In previous work by our research group [21], [28], parallel-plate excitation is combined with electrostatic levitation to make a robust pressure switch. Snap-through bi-stability of a clamped-clamped MEMS arch is another nonlinear phenomenon that could be used as a mechanism to establish a threshold pressure [23], [29]. The caveat to this approach is that the fabrication of a clamped-clamped arch beam is more challenging compared to a cantilever beam. This is because controlling residual stresses during the fabrication process is a cumbersome task [30].

In this study, we extend on previous studies [2], [31] to exploit another interesting feature of the levitation approach, which is parametric resonance-based threshold pressure sensing. A time-varying voltage on the side electrode modulates the equivalent stiffness of the system, and, under the right damping circumstance, the microbeam exhibits parametric resonance. It is shown experimentally that the dependence of parametric resonance on the damping can be used to build a threshold pressure sensor. A parametric resonance-based sensor can generate a distinct electrical signal that is easy to detect and process. This helps avoid complex

electrical circuitry and requires less processing power, which is very desirable. The proposed sensor is tunable meaning that the threshold at which the sensor is triggered can be adjusted by changing the amplitude of time-varying (AC) voltage on the side electrode. Because the beam and the bottom electrode are grounded, even if the cantilever comes into contact with the bottom electrode, it will not experience pull-in. If humidity and other environmental effects cause stiction, the sensor can be reset by applying side electrode voltage [32], [33], making the sensor robust and reusable.

The rest of this paper is organized as follows. Section II presents the working principle of the proposed sensor. In section III, a mathematical model is developed to investigate the nonlinear dynamics of the microbeam under levitation electrostatic force. The model is turned into a Mathieu's equation to demonstrate the system will experience parametric resonance. Section IV presents and discusses the experimental results. In Section V, the highlights of the work is summarized and some concluding remarks are presented.

II. PRINCIPLE OF OPERATION

The sensor is built from a micro cantilever that is subjected to the levitation electrostatic force. The microbeam is built with the POLYMUMPs fabrication standard (Fig. 1 (b)). The dimensions of microbeam and other electrodes are given in Table I. We have used QP-QFN44-7MM-.5MM package from Quik-pak Company for the MEMS chip.

The sensor is placed in an environment where it will be measuring pressure. A time-varying voltage that has DC and AC components is applied to the side electrodes and the microbeam is excited at twice its natural frequency. It is important to note that the natural frequency of the microstructure depends on the stiffness, which in this case, consists of the structural stiffness as well as the electrostatic field induced stiffness (electrical stiffness). The structural stiffness of the microstructure comes from the elasticity of the microbeam, which depends on the material and the geometry of the microbeam. The electrical stiffness is introduced mainly from the DC voltage on the side electrodes and depends on the electrode dimensions and their configuration, especially the gap between the side and the bottom electrodes.

In general, the electrical stiffness in the levitation approach increases with the bias voltage on the side electrodes. Depending on the geometry of the electrodes and their configuration, it is possible for the natural frequency to initially decrease with an increase in the bias voltage up to a certain voltage and then to increase. The increase of linear natural frequency with the DC voltage is a characteristic of the levitation approach that is in contrast to the parallel-plate configuration. A comprehensive study of the effect of bias voltage on the resonance frequency of the microcantilever is given in [11].

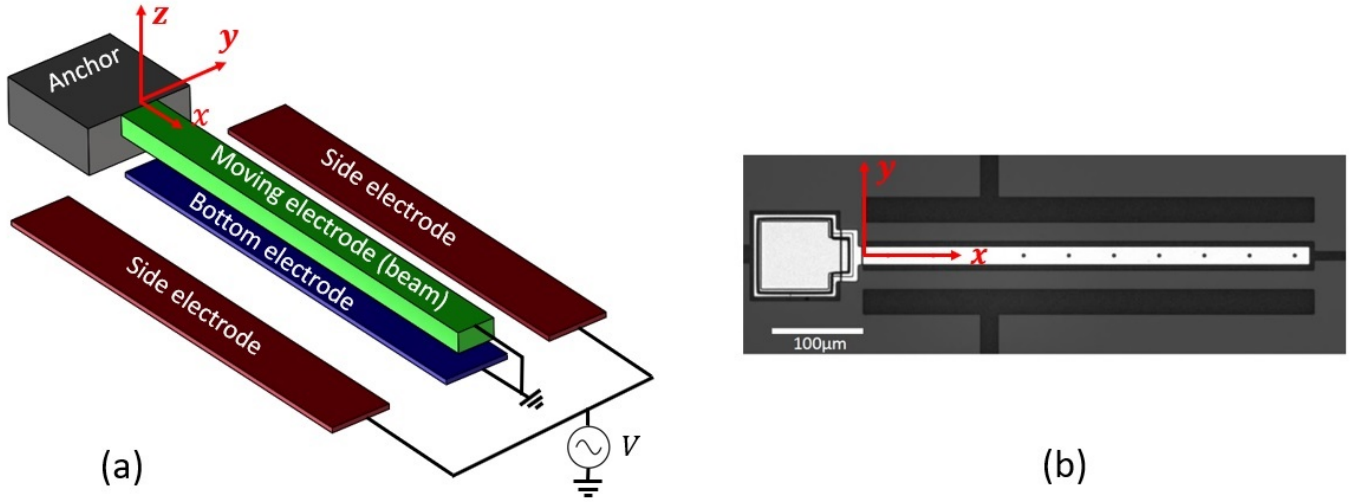


Fig. 1. (a) Schematic of the electrodes in the electrostatic levitation configuration. This particular voltage distribution creates an electric field that causes an upward electrostatic force on the moving electrode, pulling it away from the bottom electrode. (b) Top view of a fabricated microbeam. The fabrication is done using POLYUMUMPs standard.

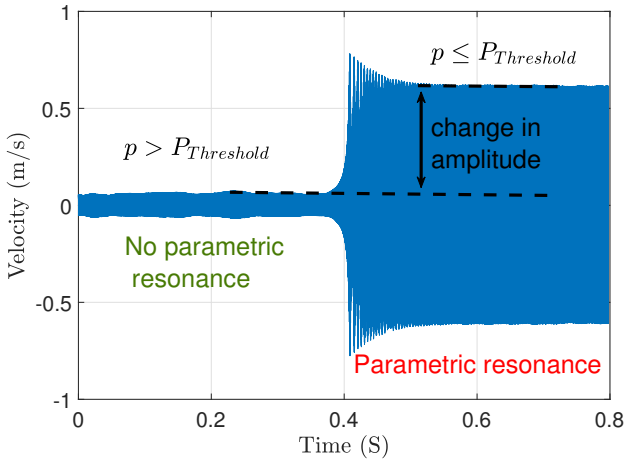


Fig. 2. Appearance of parametric resonance in the microstructure's response that leads to a distinct difference in the vibration amplitude of the microbeam. This change in the amplitude can be used to build a threshold pressure sensor.

As it will be shown experimentally, at a given DC voltage, the AC component of the voltage determines the threshold pressure at which the parametric resonance is triggered. As the microbeam is resonating, if the pressure inside the environment drops below a certain level, the parametric resonance is triggered. As a result, the amplitude of vibration will increase dramatically, and the sensor goes to the ON state. Figure 2 shows the velocity of the microbeam at its tip point before and after the parametric resonance. The increase in the amplitude is distinct and could be detected by a piezoelectric transducer or capacitive sensing between the beam and side electrodes.

III. MATHEMATICAL MODEL

A. Governing Equation of Motion

In this section, a mathematical model is developed to investigate the nonlinear dynamics of the microbeam at the parametric resonance. The governing equation of motion for the beam in the z direction (\hat{w}) is given in Eq. (1) using the Euler-Bernoulli beam theory. The microbeam is made of polysilicon, and its modulus of elasticity and density are given in Table I.

$$\rho A \frac{\partial^2 \hat{w}}{\partial t^2} + \hat{c} \frac{\partial \hat{w}}{\partial t} + EI \frac{\partial^4 \hat{w}}{\partial x^4} = V^2 \hat{f}_e(\hat{w}) \quad (1)$$

In Eq. (1), I is the second moment of inertia of the y - z section of the beam about the y axis, V is the electric voltage on the side electrode, and \hat{f}_e is the electrostatic force per unit length for when $V = 1 \text{ Volt}$. The electrostatic force profile (\hat{f}_e) is obtained from a finite element simulation in COMSOL for a 2D cross section of the beam and electrodes. A polynomial function is fit to the numerical results for force profile from COMSOL [11].

Using non-dimensional parameters given in Table II, Eq. (1) can be rewritten as:

$$\frac{\partial^2 w}{\partial t^2} + c \frac{\partial w}{\partial t} + \frac{\partial^4 w}{\partial x^4} = \frac{L^4}{EIh} V^2 \sum_{n=0}^9 A_n h^n w^n \quad (2)$$

where A_n are the coefficients of the polynomial for the force profile given in Table I. The value of c is given in Table II as well. The voltage on the side electrode is represented by V in Eq. (2), which has a DC component and a harmonic time-varying component as (3).

$$V = V_{dc} + V_{ac} \cos(\Omega T t) \quad (3)$$

where Ω is the excitation frequency.

TABLE I
 BEAM MATERIAL AND GEOMETRIC PROPERTIES

Parameter	Symbol	Value
Beam Length (μm)	L	504.25
Beam Width (μm)	b	18
Beam thickness (μm)	h	2
Beam Electrode Gap (μm)	g	2
Electrode Gap (μm)	s	20.5
Bottom electrode Width (μm)	$b1$	31
Side electrode Width (μm)	$b2$	28
Electrode Thickness (μm)	$h1$	0.5
Elastic Modulus (GPa)	E	157
Density ($\frac{\text{kg}}{\text{m}^3}$)	ρ	2330
Moment of inertial (m^4)	I	$\frac{bh^3}{12}$
Poisson's Ratio	ν	0.22
Force Constant	A_0	1.1629×10^{-7}
Force Constant	A_1	5.6299×10^{-3}
Force Constant	A_2	-1.6118×10^3
Force Constant	A_3	1.2729×10^8
Force Constant	A_4	-3.0638×10^{12}
Force Constant	A_5	-3.4096×10^{17}
Force Constant	A_6	3.6121×10^{22}
Force Constant	A_7	-1.5228×10^{27}
Force Constant	A_8	3.1435×10^{31}
Force Constant	A_9	-2.6096×10^{35}

 TABLE II
 NON-DIMENSIONALIZATION

Parameter	Substitution
x-direction position	$x = \frac{\hat{x}}{L}$
z-direction position	$w = \frac{\hat{w}}{h}$
Time	$t = \frac{\hat{t}}{T}$
Damping	$c = \frac{\hat{c}L^4}{EI^2T}$
Quality factor	$Q = \frac{\beta_1^4}{c}$
Time Constant	$T = \sqrt{\frac{\rho AL^4}{EI}}$
β_1	1.875
σ_1	0.7341
D_1	0.5
$Q(P = 590\text{mTorr})$	300
$Q(P = 990\text{mTorr})$	136
$Q(P = 2000\text{mTorr})$	67

A reduced-order model can be developed using separation of variables as

$$w(x, t) = \sum_{i=1}^n q_i(t) \phi_i(x) \quad (4)$$

where $q_i(t)$ are the time-dependent coefficients and $\phi_i(x)$ are the linear mode shapes of the cantilever given as follows

$$\phi_i(x) = D_i (\cosh(\beta_i x) - \cos(\beta_i x) - \sigma_i (\sinh(\beta_i x) - \sin(\beta_i x))) \quad (5)$$

where β_i are the square roots of the non-dimensional mechanical natural frequencies, and σ_i are constants determined from the clamped-free boundary conditions for the microcantilever. The first mode approximation is used for the analysis as it has shown good agreement with experimental results for this system in a previous study [11]. Values of β_1 , σ_1 , and D_1

for the first mode are given in Table I. The mode shapes are normalized such that the displacement at the free end is unity.

Substituting Eq. (4) into Eq. (2), multiplying both sides of Eq. (2) by ϕ_1 , and integrating between 0 and 1 using the orthogonality of the mode shapes yields a nonlinear ordinary differential equation on the time-dependent coefficient $q(t)$ as

$$\ddot{q}(t) + c\dot{q}(t) + \beta_1^4 q(t) = r_1 (V_{dc} + V_{ac} \cos(\Omega T t))^2 \sum_{n=0}^9 p_n (q(t))^n \quad (6)$$

where

$$r_1 = \frac{L^4}{EIhI_1} \quad I_1 = \int_0^1 \phi_1^2(x) dx \quad p_n = A_n h^n \int_0^1 \phi_1^{n+1} dx \quad (7)$$

The shooting method is used to solve Eq. (6) and obtain the frequency response. This method shoots for periodic solutions of the equation, and it is more computationally efficient compared to integrating Eq. (6) over time. The details of this method for the electrostatically levitating system are outlined in [11]. By performing multiple frequency sweeps at different V_{ac} and damping conditions, the transition curves will be extracted. The damping coefficient, c in Eq. (6), will be identified from the experimental results presented in Section IV.

B. Analytical Expression for Transition Curves

In addition to the numerical results from the shooting-method solution of Eq. (6), an analytical expression of the transition curves is also extracted. The transition curves separate the stable regions from unstable regions where the parametric resonance occurs. As it will be shown, the transition curves depend on the amplitude of the time-varying voltage (V_{ac}), the excitation frequency (Ω), and the damping coefficient (c) (or the quality factor (Q)). Although numerical methods can be used to solve Eq. (6) to obtain the transition curves, they are computationally cumbersome and time consuming. To obtain the transition curves, the frequency response of Eq. (6) should be calculated at different electrical excitations (V_{dc} and V_{ac}) and different damping conditions, which is a cumbersome task. On the other hand, an analytical formula for the transition curves not only yields the results with much less computation, but it provides insight on how the dynamics of the system is affected by the intertwined relationship between various parameters, and therefore it is very useful.

To obtain the transition curves, one can rewrite Eq. (6) into the form of Mathieu's equation given below.

$$\ddot{q}_d(t) + C\dot{q}_d(t) + [\delta + \epsilon \cos \tau] q_d(t) = 0 \quad (8)$$

Introducing a change of variable given as

$$q(t) = q_{st} + q_d(t), \quad (9)$$

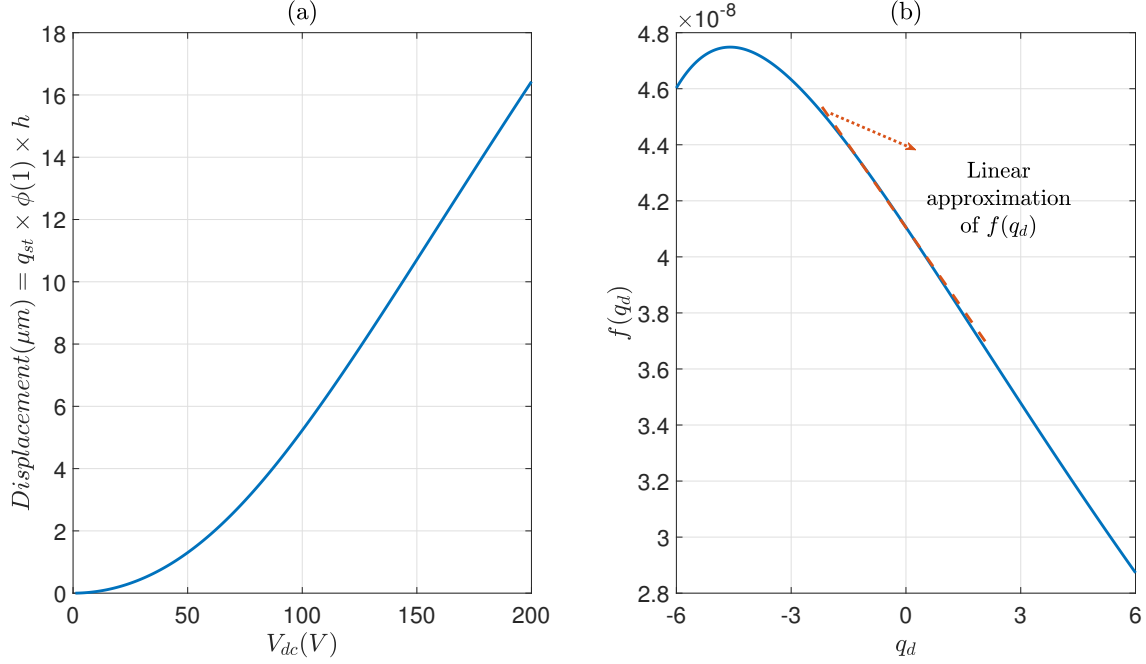


Fig. 3. (a) The solution of Eq. (11) gives the static displacement at the tip of the beam for different DC voltages on the side electrodes (b) The linearization of the electrostatic force about $q_d = 0$ given in Eq. (12). According to this figure, the linearization of the electrostatic force is a reasonable assumption.

one can rewrite Eq. (6) as

$$\ddot{q}_d(t) + c\dot{q}_d(t) + \beta_1^4 q_d(t) = r_1 (V_{dc} + V_{ac} \cos(\Omega T t))^2 \sum_{n=0}^9 p_n (q_{st} + q_d(t))^n - \beta_1^4 q_{st} \quad (10)$$

where q_{st} is the solution of the algebraic static equation, given in Eq. (11). Figure 3 (a) shows the static displacement of the microcantilever at the tip point as the voltage on the side electrodes increases.

$$\beta_1^4 q_{st} = r_1 (V_{dc})^2 \sum_{n=0}^9 p_n (q_{st})^n \quad (11)$$

The summation in Eq. (10), which is a function of q_d , can be expanded about $q_d = 0$ using Taylor series expansion as

$$f(q_d) = \sum_{n=0}^9 p_n (q_{st} + q_d(t))^n = \alpha_0 + \alpha_1 q_d + O(q_d^2) \quad (12)$$

where

$$\alpha_0 = f(0) = \sum_{n=0}^9 p_n (q_{st})^n \quad \alpha_1 = \frac{\dot{f}(0)}{1!} = \sum_{n=0}^9 n p_n (q_{st})^{n-1} \quad (13)$$

Substituting Eq. (12) into Eq. (10) and rearranging the terms, one can write

$$\ddot{q}_d(t) + \frac{\beta_1^2}{Q} \dot{q}_d(t) + [(\beta_1^4 - \delta_1) - \epsilon_{11} \cos(\Omega T t) - \epsilon_{21} \cos(2\Omega T t)] q_d(t) = [(\delta_0 - \beta_1^4 q_{st}) + \epsilon_{10} \cos(\Omega T t) + \epsilon_{20} \cos(2\Omega T t)] + [\delta_2 + \epsilon_{12} \cos(\Omega T t) + \epsilon_{22} \cos(2\Omega T t)] O(q_d^2) \quad (14)$$

where Q is the quality factor given in Table II. All the other coefficients in Eq. (14) are given in the Appendix. In Eq. (14), the higher-order terms are ignored, ($O(q_d^2)$). That serves as a good approximation because the electrostatic force ($f(q_d)$) is mostly linear about the static solutions corresponding to high DC voltages as shown in Fig. 3 (b). This figure illustrates that at the q_{st} corresponding to 165(V) on the side electrodes, the electrostatic force can be approximated with a line. All of the experiments are performed at this voltage. To obtain the transition curves, the homogeneous version of Eq. (14) is considered. The last assumption to make is to ignore the $\epsilon_{21} \cos(2\Omega T t)$ term in Eq. (14) compared to the $\epsilon_{11} \cos(\Omega T t)$ term. This is a reasonable approximation when V_{ac} is much smaller than V_{dc} as shown in the equation below.

$$\frac{\epsilon_{21}}{\epsilon_{11}} = \frac{V_{ac}}{4V_{dc}} \quad (15)$$

Using another change of variable given in Eq. (16), and applying the assumptions explained above, Eq. (14) can be rewritten in the form of Mathieu's equation as given in Eq. (17).

$$\Omega T t = \tau \quad (16)$$

$$\ddot{q}_d(t) + C_M \dot{q}_d(t) + [\delta_M + \epsilon_M \cos \tau] q_d(t) = 0 \quad (17)$$

where C_M , δ_M , and ϵ_M are given in the Appendix.

For the Mathieu's equation given in Eq. (17), the transition curves are obtained by using perturbation techniques, and they are given by the following expression [34].

$$\delta_M = \frac{1}{4} \pm \frac{\sqrt{\epsilon_M^2 - c_M^2}}{2} + O(\epsilon_M^2) \quad (18)$$

Substituting all the coefficients in the equation for the transition curves results in:

$$\frac{\beta_1^4 - r_1 \alpha_1 (V_{dc}^2 + \frac{V_{ac}^2}{2})}{(\Omega T)^2} = \frac{1}{4} \mp \left(\frac{2r_1 \alpha_1 V_{dc} V_{ac}}{(\Omega T)^2} \right) \frac{\sqrt{(\frac{2r_1 \alpha_1 V_{dc} V_{ac}}{(\Omega T)^2})^2 - (\frac{\beta_1^2}{Q \Omega T})^2}}{2} + O(\epsilon_M^2) \quad (19)$$

which is an implicit algebraic equation relating the V_{ac} , quality factor (Q), and the excitation frequency (Ω). In the next section, the prediction of this equation for the transition curves is shown and compared with the experimental results.

IV. EXPERIMENTAL RESULTS AND DISCUSSION

The experimental set up is shown in Fig. 4. The sensor is placed inside a chamber with controlled pressure. All the experiments are conducted in the room temperature ($25^\circ C$). The beam is excited by applying a voltage with DC and AC components to the side electrodes. The velocity of the beam at its free end is measured with a Polytec MSA 500 laser vibrometer. To demonstrate the parametric resonance of the microbeam, a forward and backward frequency sweep is conducted at a constant pressure of $P = 590 \text{ mTorr}$ when the DC voltage on the side electrodes is 165 V . Figure 5 (a) presents the results for when the AC voltage is 10 V . As shown in this figure, there is a frequency band (Δf) where the beam undergoes parametric excitation. The branch associated with parametric excitation expands well beyond this frequency band. However, reaching the points outside of this frequency band depends on the initial conditions of the beam. For reliable and consistent operation of the sensor, we only focus on this frequency band, where, independent of initial conditions, the beam is forced to undergo parametric excitation.

The frequency band in Fig. 5 (a) depends on the amplitude of the AC voltage on the side electrode. As shown in Fig. 5 (b) and Fig. 6, this frequency band expands with an increase in the AC voltage. The curve in Fig. 5 (b), which is called a transition curve (or instability tongue), separates the stable and unstable regions depending on the emergence of parametric resonance. This figure illustrates that there is a minimum value for the AC voltage below which the beam will not experience parametric resonance. This minimum point is strongly dependent on the pressure inside the chamber. Figure

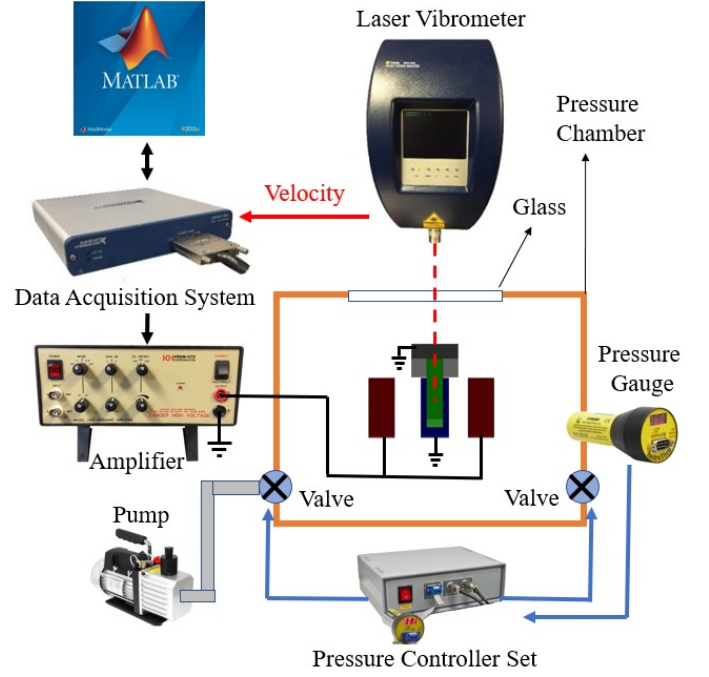


Fig. 4. The experimental setup. The microbeam is excited by applying voltage to the side electrodes. The velocity of the microbeam is measured with a laser vibrometer. The pressure inside the chamber is controlled via a pressure controller set. By reducing the pressure inside the chamber, the microbeam exhibits large amplitude vibrations because of parametric resonance.

7 shows the transition curves for three different pressures. The minimum AC voltage required to trigger the parametric resonance increases with the pressure (Fig. 8). That indicates the energy dissipation that system needs to overcome before the parametric resonance can occur.

As depicted in Fig. 7, the transition curves obtained from the simulations are in good agreement with the experimental results. The damping coefficient in Eq. (6) is identified from matching the minimum points of the transition curves obtained from the experiment and shooting method. Furthermore, this figure shows that the transition curves that are given by the analytical perturbation method (Eq. (19)) are in excellent agreement with the results from the shooting methods. For these transition curves, we have used the same quality factor that was identified by comparing the results of the shooting method to the experiment. The numerical values of the quality factors at each pressure are given in the Table II. Substituting the values of quality factors into Eq. (19) yields an implicit algebraic equation between V_{ac} and Ω , which is plotted with MATLAB. Solving these algebraic equations are computationally more efficient than the numerical method of shooting that solves the nonlinear differential equation. The transition curves from the model are all symmetric, where as the experimental ones are slightly bent to the right. This could be attributed to the stiffness and damping of the air which is not considered in the model. Because of the large vibration of the beam at the parametric resonance, the air stiffness because of the squeeze film effect could be considerable and needs further investigations.

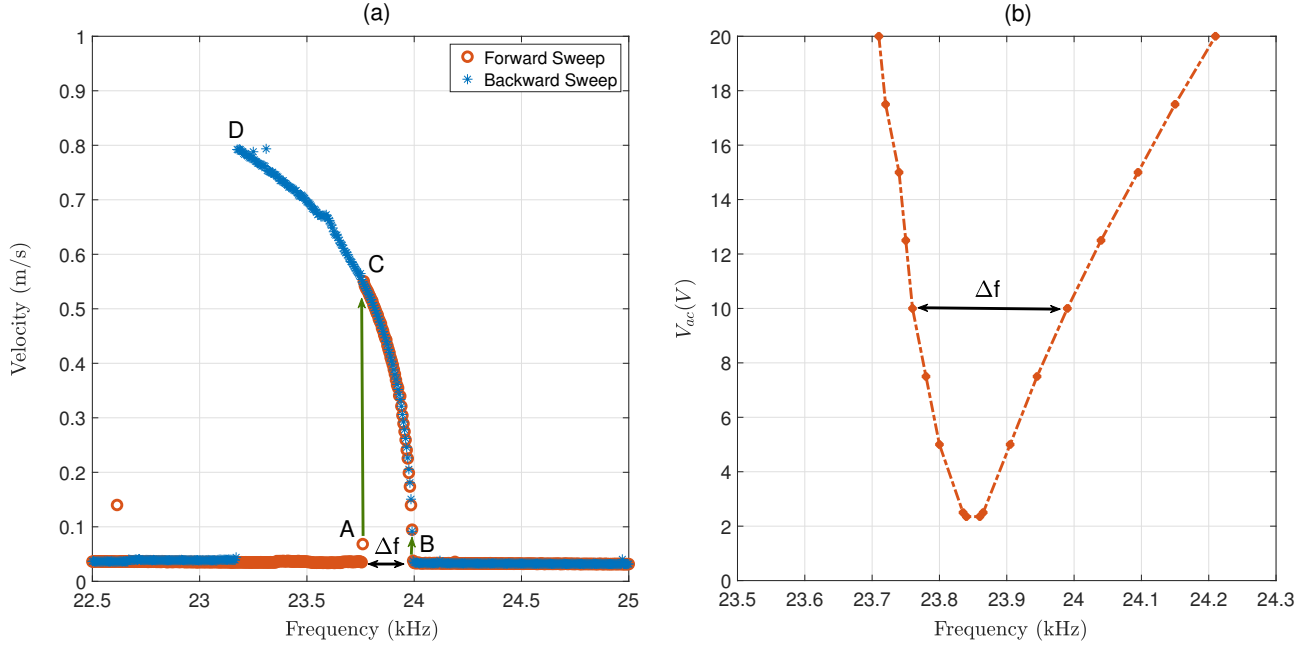


Fig. 5. (a) Forward and backward frequency sweeps at $V_{dc} = 165(V) - V_{ac} = 10(V) - P = 590(mTorr)$. The jump in the amplitude on the left side of the instability region is much more pronounced compared to the jump on the right side. (b) The transition curve at $V_{dc} = 165(V) - P = 590(mTorr)$. Inside the transition curve lies the frequency region for which the beam exhibits parametric resonance. Below a certain V_{ac} there will be no parametric resonance.

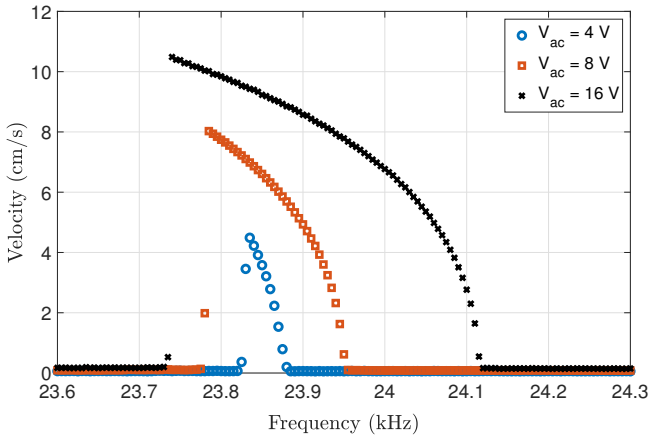


Fig. 6. Forward frequency sweeps at $V_{dc} = 165(V) - P = 900(mTorr)$ and different V_{ac} . As shown in Fig. 5, the frequency range that is used to obtain the transition curve, can be extracted by performing only the forward frequency sweep. This frequency range enlarges by increasing V_{ac} .

stiffness and damping effect, which causes similar deviations on the left side of the transition curve in Fig. 7. The best performance of the sensor is obtained when it is operated at an AC voltage and a frequency (V_{ac}, f) corresponding to points on the left side of the transition curves. This is because the jump in the amplitude on the left side of the instability region (point A in Fig. 5 (a)) is much larger than the jump on the right side (point B in Fig. 5 (a)). Operating the sensor at this (V_{ac}, f) ensures a large change in the amplitude when the parametric resonance is triggered. Figure 10 illustrates how the transition curve grows by decrease in pressure. The operating point which is initially outside of the transition curve, will be encompassed by the growing transition curve as the pressure drops. That means, if the pressure drops in the environment by a very small amount, the oscillations will significantly increase. This significant rise in the amplitude can be observed using a charge amplifying circuit, which can detect the capacitance change. This study has characterized the pressure sensor in pressure ranges below 2 Torr. Studying the performance of the pressure sensor at pressures above 2 Torr can be the subject of future investigations.

To present the operating voltages of the pressure sensor, the minimum AC voltages required to trigger parametric resonance at 23.8kHz for different pressures are shown in Figure 9. The figure compares simulations with experimental results. Based on this figure, the AC voltage can be tuned to establish different threshold pressure values. The operating DC voltage is fixed at 165 V. The difference between the experimental and simulation results is related to the air

In theory, the sensor could be used to detect either drop or rise in pressure. However, we have studied the device only to detect a drop-in pressure below a certain threshold. The application of the sensor for detecting a rise in pressure above a threshold value needs further investigation and could be studied in a future work. This is because for the sensor to detect a pressure rise, we need to change the operating point of the sensor. In Fig. 11, we have demonstrated the

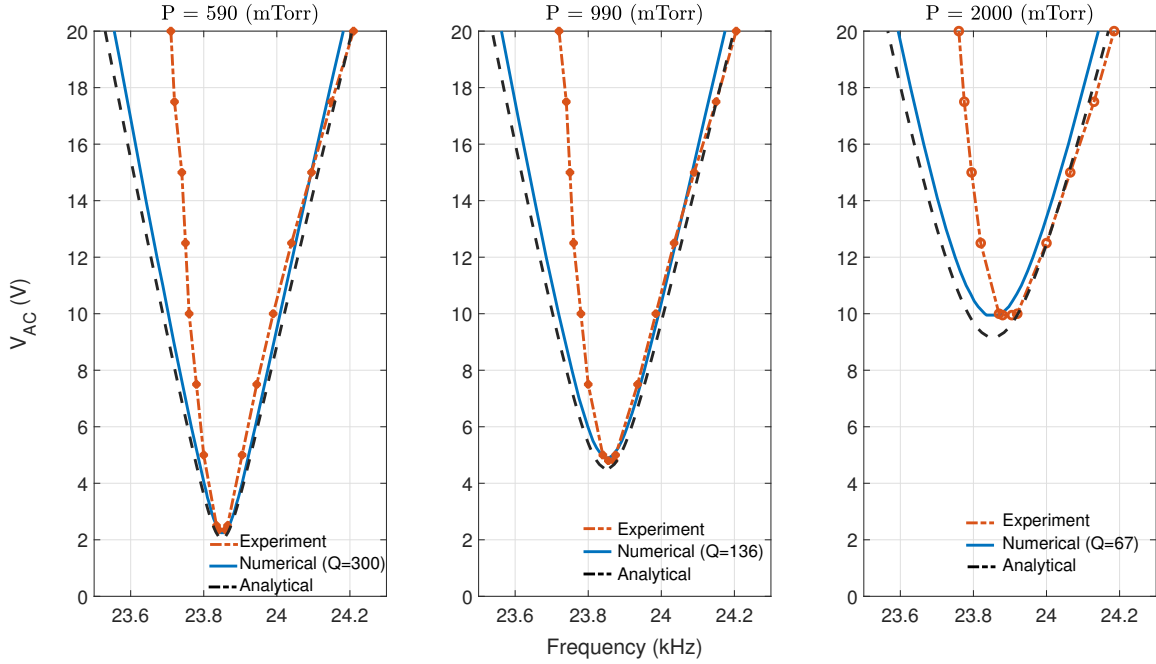


Fig. 7. Transition curves for three different pressure values. By increasing the pressure the transition curve shrinks, and therefore the minimum voltage for the appearance of the parametric resonance increases. The center-line indicates the experimental results, while the dashed line shows the analytical solution and the solid line depicts the numerical simulation data obtained from the shooting technique.

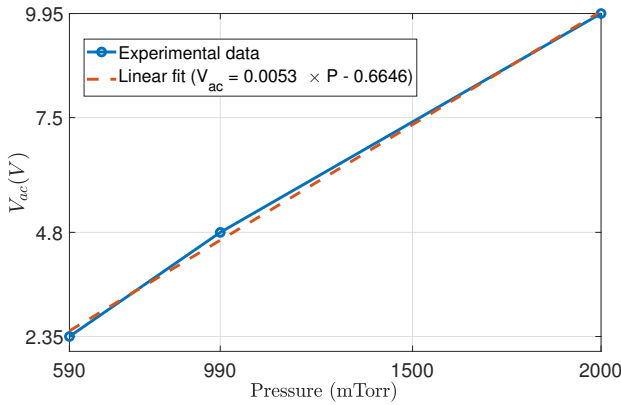


Fig. 8. The minimum AC voltage required to trigger parametric resonance increases with pressure.

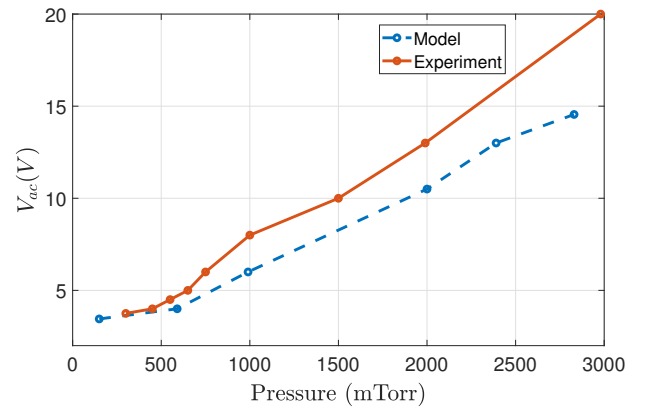


Fig. 9. Red (Solid-dot) curve: The Minimum experimental V_{ac} required for the appearance of parametric resonance at different pressures ($V_{dc} = 165(V)$). Blue (dash-dot) curve: The minimum theoretical V_{ac} to trigger parametric resonance when the excitation frequency is $23.8(kHz)$ ($V_{dc} = 165(V)$). This curve can be used for the operation of the sensor to establish different pressure thresholds when detection of drop in the pressure is desired. At each pressure, the required V_{ac} for the operation of the sensor can be identified from this curve.

difference between detecting a pressure drop versus detecting a pressure rise by schematically showing the forward and backward frequency sweeps at different pressures. If the sensor is operating at point A shown in the Fig. 11, a drop in pressure will trigger the parametric resonance and the amplitude jumps up to point B. But if the pressure increases, the amplitude will not fall back to point A. It rather gradually sinks down to point C and there would be no sudden jump down similar to the jump up. A better operating point for detecting the pressure rise is point D that exists at the end of the high branch oscillation for the backward frequency sweep. When the sensor operates at point D at low pressure, the sensor will have a large amplitude. If the sensor experiences

a pressure rise, the amplitude will drop suddenly to point E. This distinct drop in amplitude because of pressure rise can easily be realized in a charge amplifying circuit for capacitance detection.

V. CONCLUSION

A threshold pressure sensor is proposed using parametric resonance in a microbeam subjected to the levitation

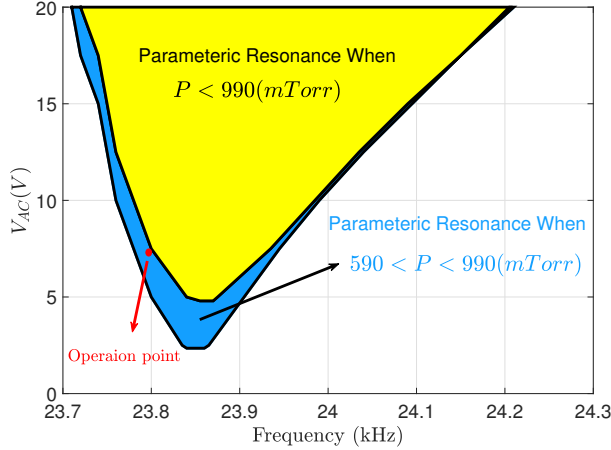


Fig. 10. By operating the sensor at a frequency and V_{ac} outside of the transition curves for a particular pressure (the operation point), the sensor does not experience parametric resonance. With a decrease in pressure, the transition curve grows and encompasses the operation point. Therefore, the sensor will exhibit parametric resonance.

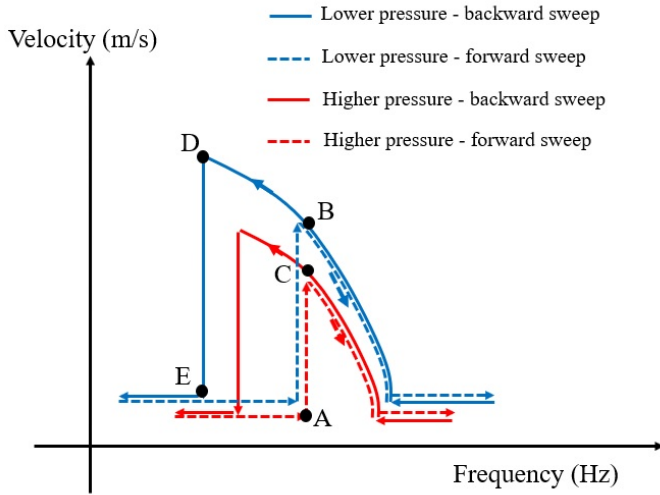


Fig. 11. The forward and backward frequency sweeps are shown at two pressure levels schematically. This figure shows that for detecting a rise in pressure, the sensor should be operated at point D, where an increase in pressure will lead to a dramatic drop in the amplitude of vibration.

electrostatic force. The experimental data shows the distinct difference in the vibration amplitude of the beam when it is parametrically excited compared to when it is not. The appearance of the parametric resonance depends on the pressure and AC voltages. Therefore, the AC voltage can be used as a tuning parameter to establish different values for the threshold pressure. The sensor is reusable, and in theory, it can be used to detect when the pressure goes above or drops below a certain threshold. The operation of the sensor for detecting a drop in pressure is studied experimentally and theoretically. The application of the sensor for detecting rise in the pressure needs further investigations. A mathematical model is developed using the Euler-Bernoulli beam theory. The governing equation of motion is solved using the shooting

method, and the results are compared to the experimental data. An analytical expression for the transition curves of the system is obtained by rewriting the governing equation of motion in the form of Mathieu's equation. The comparison shows that the developed model is capable of capturing the nonlinear dynamics of the system that can serve in designing high signal-to-noise ratio sensors with improved pressure sensing resolution.

ACKNOWLEDGMENT

The authors would like to acknowledge the financial support of this study by the National Science Foundation (NSF) through grant #ECCS1608692.

VI. APPENDIX

$$\delta_0 = r_1 \alpha_0 \left(V_{dc}^2 + \frac{V_{ac}^2}{2} \right) \quad (20)$$

$$\epsilon_{10} = 2r_1 \alpha_0 V_{dc} V_{ac} \quad (21)$$

$$\epsilon_{20} = \frac{r_1 \alpha_0 V_{ac}^2}{2} \quad (22)$$

$$\delta_1 = r_1 \alpha_1 \left(V_{dc}^2 + \frac{V_{ac}^2}{2} \right) \quad (23)$$

$$\epsilon_{11} = 2r_1 \alpha_1 V_{dc} V_{ac} \quad (24)$$

$$\epsilon_{21} = \frac{r_1 \alpha_1 V_{ac}^2}{2} \quad (25)$$

$$\delta_2 = r_1 \left(V_{dc}^2 + \frac{V_{ac}^2}{2} \right) \quad (26)$$

$$\epsilon_{12} = 2r_1 V_{dc} V_{ac} \quad (27)$$

$$\epsilon_{22} = \frac{r_1 V_{ac}^2}{2} \quad (28)$$

$$c_M = \frac{\beta_1^2}{Q\Omega T} \quad (29)$$

$$\delta_M = \frac{\beta_1^4 - \delta_1}{(\Omega T)^2} \quad (30)$$

$$\epsilon_M = -\frac{\epsilon_{11}}{(\Omega T)^2} \quad (31)$$

$$\delta_0 = r_1 \alpha_1 \left(V_{dc}^2 + \frac{V_{ac}^2}{2} \right) \quad (32)$$

REFERENCES

- [1] K. Moran, C. Burgner, S. Shaw, and K. Turner, "A review of parametric resonance in microelectromechanical systems," *Nonlinear Theory and Its Applications, IEICE*, vol. 4, no. 3, pp. 198–224, 2013.
- [2] M. Pallay and S. Towfighian, "A parametric electrostatic resonator using repulsive force," *Sensors and Actuators A: Physical*, vol. 277, pp. 134–141, 2018.
- [3] C. Guo, E. Tatar, and G. K. Fedder, "Large-displacement parametric resonance using a shaped comb drive," in *2013 IEEE 26th International Conference on Micro Electro Mechanical Systems (MEMS)*, 2013, pp. 173–176.
- [4] Y. Linzon, B. Ilic, S. Lulinsky, and S. Krylov, "Efficient parametric excitation of silicon-on-insulator microcantilever beams by fringing electrostatic fields," *Journal of Applied Physics*, vol. 113, no. 16, p. 163508, 2013.
- [5] Wenhua Zhang, R. Baskaran, and K. L. Turner, "Changing the behavior of parametric resonance in mems oscillators by tuning the effective cubic stiffness," in *The Sixteenth Annual International Conference on Micro Electro Mechanical Systems, 2003. MEMS-03 Kyoto. IEEE*, 2003, pp. 173–176.
- [6] M. Ozdogan, M. Daeichin, A. Ramini, and S. Towfighian, "Parametric resonance of a repulsive force mems electrostatic mirror," *Sensors and Actuators A: Physical*, vol. 265, 2017.
- [7] D. I. Caruntu and E. Juarez, "Voltage effect on amplitude–frequency response of parametric resonance of electrostatically actuated double-walled carbon nanotube resonators," *Nonlinear Dynamics*, vol. 98, 2019.
- [8] Wenhua Zhang and K. L. Turner, "A mass sensor based on parametric resonance," *A Solid State Sensor, Actuator and Microsystems Workshop, Hilton Head Island, South Carolina, June 6–10, 2004*.
- [9] Wenhua Zhang and K. L. Turner, "Application of parametric resonance amplification in a single-crystal silicon micro-oscillator based mass sensor," *Sensors and Actuators A: Physical*, vol. 122, no. 1, pp. 23–30, 2005.
- [10] Ki Bang Lee and Young-Ho Cho, "Laterally driven electrostatic repulsive-force microactuators using asymmetric field distribution," *Journal of Microelectromechanical Systems*, vol. 10, no. 1, pp. 128–136, March 2001.
- [11] M. Pallay, M. Daeichin, and S. Towfighian, "Dynamic behavior of an electrostatic mems resonator with repulsive actuation," *Nonlinear Dynamics*, vol. 89, no. 2, p. 1525–1538, 2017.
- [12] M. Daeichin, R. N. Miles, and S. Towfighian, "Experimental characterization of the electrostatic levitation force in mems transducers," *Journal of Vibration and Acoustics*, vol. 142, no. 4, 2020.
- [13] M. Pallay, R. N. Miles, and S. Towfighian, "Merging parallel-plate and levitation actuators to enable linearity and tunability in electrostatic mems," *Journal of Applied Physics*, vol. 126, no. 1, p. 014501, 2019.
- [14] S. Towfighian, S. He, and R. Ben Mrad, "A low voltage electrostatic micro actuator for large out-of-plane displacement," *8th International Conference on Micro- and Nanosystems*, 08 2014.
- [15] M. Daeichin, M. Ozdogan, S. Towfighian, and R. N. Miles, "Dynamic response of a tunable mems accelerometer based on repulsive force," *Sensors & Actuators: A. Physical*, vol. 289, pp. 34–43, 2019.
- [16] M. Ozdogan, S. Towfighian, and R. N. Miles, "Fabrication and experimental characterization of a mems microphone using electrostatic levitation," in *2019 IEEE SENSORS*, 2019, pp. 1–4.
- [17] M. Daeichin, S. Towfighian, and R. N. Miles, "Lateral pull-in instability of mems transducers employing repulsive force," *Nonlinear Dynamics*, pp. 1927–1940, 2020.
- [18] M. Ozdogan, S. Towfighian, and R. N. Miles, "Modeling and characterization of a pull-in free mems microphone," *IEEE Sensors Journal*, vol. 20, no. 12, pp. 6314–6323, 2020.
- [19] K. Bruckner, V. Cimalla, F. Niebelschutz, R. Stephan, K. Tonisch, O. Ambacher, and M. A. Hein, "Gas pressure sensing based on mems resonators," in *SENSORS, 2007 IEEE*, 2007, pp. 1251–1254.
- [20] Z. Zhang, Yan-Hong Zhang, L. Liu, and Tian-Ling Ren, "A novel mems pressure sensor with mosfet on chip," in *SENSORS, 2008 IEEE*, 2008, pp. 1564–1567.
- [21] M. Pallay, R. N. Miles, and S. Towfighian, "A tunable electrostatic mems pressure switch," *IEEE Transactions on Industrial Electronics*, pp. 1–1, 2019.
- [22] Y. D. Yukang Yang and Y. Li, "Buckling of piezoelectric sandwich microplates with arbitrary in-plane bcs rested on foundation: effect of hygro-thermo-electro-elastic field," *The European Physical Journal Plus*, vol. 135, no. 1, 2020.
- [23] M. H. Hasan, F. M. Alsaleem, and H. M. Ouakad, "Novel threshold pressure sensors based on nonlinear dynamics of mems resonators," *Journal of Micromechanics and Microengineering*, vol. 28, no. 6, 2018.
- [24] R. K. Gupta and S. D. Senturia, "Pull-in time dynamics as a measure of absolute pressure," in *Proceedings IEEE The Tenth Annual International Workshop on Micro Electro Mechanical Systems. An Investigation of Micro Structures, Sensors, Actuators, Machines and Robots*, 1997, pp. 290–294.
- [25] E. M. Miandoab, H. N. Pishkenari, A. Meghdari, and M. Fathi, "A general closed-form solution for the static pull-in voltages of electrostatically actuated mems/nems," *Physica E: Low-dimensional Systems and Nanostructures*, vol. 90, pp. 7–12, 2017.
- [26] F. Najar, M. Ghommem, and A. Abdelkefi, "A double-side electrically-actuated arch microbeam for pressure sensing applications," *International Journal of Mechanical Sciences*, vol. 178, p. 105624, 2020.
- [27] W. Zhang, H. Yan, Z.-K. Peng, and G. Meng, "Electrostatic pull-in instability in mems/nems: A review," *Sensors and Actuators A: Physical*, vol. 214, pp. 187–218, 2014.
- [28] M. Pallay and S. Towfighian, "A combined mems threshold pressure sensor and switch," in *2019 IEEE SENSORS*, 2019, pp. 1–4.
- [29] *A Novel Threshold Pressure Sensor Based on Nonlinear Dynamics of MEMS Arches*, ser. International Design Engineering Technical Conferences and Computers and Information in Engineering Conference, vol. Volume 9: 13th ASME/IEEE International Conference on Mechatronic and Embedded Systems and Applications, 08 2017.
- [30] M. A. A. Hafiz, L. Kosuru, A. Ramini, K. N. Chappanda, , and M. I. Younis, "In-plane mems shallow arch beam for mechanical memory," *Micromachines*, vol. 7, no. 10, 2016.
- [31] M. N. Hasan, M. Pallay, and S. Towfighian, "Threshold pressure sensing using parametric resonance in electrostatic mems," in *2019 IEEE SENSORS*, 2019, pp. 1–4.
- [32] M. Pallay, A. I. Ibrahim, R. N. Miles, and S. Towfighian, "Pairing electrostatic levitation with triboelectric transduction for high-performance self-powered mems sensors and actuators," *Applied Physics Letters*, vol. 115, no. 13, p. 133503, 2019.
- [33] M. Pallay and S. Towfighian, "A reliable mems switch using electrostatic levitation," *Applied Physics Letter*, vol. 113, no. 21, p. 213102, 2018.
- [34] R. H. Rand, "Lecture notes on nonlinear vibrations," *Cornell University*, vol. 53, 2012.